

Impact of Ag_2O on the mechanical and shielding features of $\text{ZnO}-\text{Er}_2\text{O}_3-\text{TeO}_2$ glasses

Jamila S. Alzahrani

Princess Nourah bint Abdulrahman University

NAZIRUL NAZRIN SHAHROL NIDZAM (✉ nazirulnazrin@gmail.com)

Universiti Putra Malaysia

M. K. Halimah

Universiti Putra Malaysia

K. Mahmoud

Ural Federal University

M. I. Sayyed

Isra University

M.Y. Hanfi

Ural Federal University

M. K. Izzaty

Imperial College London

Z.A. Alrowaili

Jouf University

M. S. Al-Buriahi

Sakarya University

Imed Boukhris

King Khalid University

Imen Kebaili

King Khalid University

Research Article

Keywords: mechanical properties, Monte Carlo simulation, shielding features, tellurite glasses, cross section

Posted Date: January 14th, 2022

DOI: <https://doi.org/10.21203/rs.3.rs-1249950/v1>

License:  This work is licensed under a Creative Commons Attribution 4.0 International License. [Read Full License](#)

Abstract

The investigation involves a comprehensive study on the mechanical and shielding features of the zinc erbium tellurite glasses as a function of doped Ag_2O content. The mechanical features are estimated for the examined glasses by utilizing the Makishima-Makinzie model. The results showed the mechanical moduli of Young (E), bulk (B), Shear (K), and longitudinal (L) increased with the increment of the Ag_2O substitution ratio. Besides, the radiation shielding properties were also studied and discussed. Among the shielding parameters, the linear attenuation coefficient (LAC), half-value layer (HVL), the lead equivalent and transmission rate (TR) were estimated. The linear attenuation coefficient results illustrated that the TZEAg glasses are better compared to the commercial marketing glasses, especially TZEAg5 glasses. Doping of Ag_2O content in zinc erbium tellurite glass improves its ability to attenuate the gamma photons. Also, this study revealed the effectiveness of the examined glasses on the fast neutron, where the fast neutron mass removal cross-section \sum_R (cm^2/g) computed theoretically. The results offered the maximum value of $\sum_R = 0.019 \text{ cm}^2/\text{g}$ attained for TZEAg1 while the minimum value $\sum_R = 0.01884 \text{ cm}^2/\text{g}$ for TZEAg5 glass.

1. Introduction

Gamma-ray shielding is a very important topic across a wide range of technologies in industries ranging from medical imaging and healthcare to radiotherapy, research facilities and nuclear energy. Several principles have been developed to control the exposure to radiation doses, and one of the most popular principles is ALARA which strives to reduce the exposure of the radiation to the environment and humans [1, 2]. Considering the social and economic factors, consulting with a protection materials expert is extremely important to develop efficient solutions to the shielding needs. The choice of shielding material depends on the kind of radiation that is present. The atoms of the shielding materials interact differently with different kinds of radiation. For instance, lead is capable to shield gamma photons efficiently, but it is quite ineffective for shielding from neutrons. In general, dense materials such as lead, tungsten, heavy metal oxide glasses and certain types of alloys are the strongest in abating the gamma photons. Some types of concretes and polymers are also good materials for blocking neutron radiation [3–9]. Practically, selecting the suitable material allow the manufacturer to utilize a smaller amount of material which can save space. For example, a glass shield with relatively high density would only occupy a quarter or half of the space occupied by a commercial glass with similar attenuation ability. Transparency of a medium is also an important factor when choosing the shielding material for eyeglasses or window glasses used in the X-ray rooms. Other important factors to be considered when selecting the shielding materials are the environmental conditions, the cost of the materials, ease of shipping, handling, and installation. When planning to protect people and workers in the medical and industrial fields from radiation, the attenuation properties of different materials need to be known and the most appropriate material that provides the appropriate radiation protection should be chosen. The aforementioned factors must be considered when selecting the right medium as accurate determination of the shielding factors for different materials is an important part of any radiation shielding plan [10–12]. Cheap and eco-friendly glasses, with interesting optical and physical features, are a good choice to manufacture novel radiation shielding products. Different researchers are trying to develop a variety of thicknesses and sizes of several glass systems that is outstanding in providing radiation protection [13–19]. Radiation shielding glasses are used extensively in dental clinics, radiation therapy rooms, operating theatres, laboratories, veterinary clinics and different materials testing.

TeO_2 glasses, one of the most common glasses, hold technological and scientific importance because of their distinctive features which include good chemical durability, high refractive indices, interesting optical properties, good semiconducting properties and high dielectric constant. Also, it is reported that TeO_2 glasses have relatively high density and thus possess a good attenuation ability against gamma radiation [20–22]. During the preparation process of the TeO_2 -based glasses, some glasses modifiers such as ZnO and Ag_2O are used to enhance their optical features and radiation attenuation competences [23, 24]. Introducing the Er_2O_3 ions enhances the chemical durability of glass as well

as the radiation shielding features. Therefore, the chance for the TeO_2 glasses with Er_2O_3 to be used in several applications fields such as glass fibers optoelectronics and medical applications is promising [25, 26].

One of the most extensively used techniques for the evaluation of radiation shielding glasses performance is Monte Carlo simulation (MC) [27–29]. MC is an excellent method to study the physical and radiation shielding parameters in case the experimental preparations are difficult or limited to reach. Accordingly, this investigation is aimed to detect the mechanical, and radiation shielding features of a glass system containing TeO_2 , ZnO , Er_2O_3 and Ag_2O compounds. The Makishima-Mackenzie (M-M) model is utilized to examine the mechanical features. Moreover, the Monte Carlo N-particle transport code (MCNP-5) was applied to determine the properties of radiation shielding for the studied glass system.

2. Materials And Methods

2.1. Mechanical properties

Studying the hardness and elastic properties of the glasses is vital to achieving proper implementation of shielding materials. Therefore, the mechanical features and elastic moduli were theoretically determined for the glass system containing the TeO_2 , ZnO , Er_2O_3 and Ag_2O compounds with different ratios using the M-M model. The chemical composition (mol %), density (ρ , g/cm^3), and molar volume (V_M , cm^3/mol) of the synthetic glass samples were tabulated in Table 1 [30]. Beginning from the constating compounds dissociation energy G_i , the total dissociation energies (G_t , kJ/cm^3) were computed for the examined glass samples. The packing factor (V_i , cm^3/mol) was also estimated for the studied TZEAg glasses. The packing density (V_t) depends on The molecular weight (M_W , g/mol), the molar fraction (x_i), and the predicted values for V_i where $V_t = (\rho/M_w) \sum v_i x_i$. Then, the elastic moduli Young (Y , GPa), bulk (B , GPa), shear (S , GPa), and longitudinal (L , GPa) were computed by utilizing the expected values of V_t and G_t , where $Y=2V_tG_t$, $B=1.2 V_t Y$, $S=(3EB)/(9B-E)$, and $L=B+0.75S$. Furthermore, the Poisson ratio (σ) estimated from $\sigma = 0.5-0.1388V_t$ and the micro hardness (H , GPa) based on the calculated σ values, where $H= (1-2 \sigma)/ (6(1 + \sigma))$. The softening temperature (T_s), ultrasonic velocities (V_l and V_s), and fractal bond connectivity (d) were estimated as well [31].

Table 1
Chemical composition, density, molar volume of TZEAg glass samples.

	Chemical composition (wt %)				
	TZEAg1	TZEAg2	TZEAg3	TZEAg4	TZEAg5
Ag_2O	1.58	3.14	4.68	6.20	7.71
Er_2O_3	10.32	10.15	9.99	9.83	9.67
TeO_2	72.30	71.16	70.03	68.91	67.80
ZnO	15.80	15.55	15.30	15.06	14.82
Molecular weight	146.85	147.70	148.56	149.42	150.28
Molar volume	32.85	32.25	31.54	31.00	30.24

2.2. Shielding capacity

The MCNP-5 code was employed to detect the protection factors of the TZEAg glass samples. The released photons average track length (ATL) was simulated in the energy interval between 0.240 and 1.408 MeV. An input file was built to reach the essential target. An input file was created to achieve the required target. Figure 1 exhibited the 3D geometry that represents the generated input file. The 3D geometry demonstrates a large lead cylinder with a maximum of 500 mm and

a diameter of 200 mm. This cylinder is applied to block the photons from leaving outside the geometry and shield geometry from the surrounding background radiations. Inside this big cylinder, the source of radioactive was installed in the center of this cylinder at point (0, 0, 0). The type of source, radioactivity distribution, dimensions, and emission direction were added to the source card (SDEF). The photons released by the radioactive source were directed to the TZEAg glass samples utilizing a cylindrical collimator of lead with the highest of 70 mm and diameter of 10 mm. The collimator includes a vertical slit with a diameter of 10 cm to collimate the emitted photons. The chemical composition and density of the examined glass samples were noted in Table 1. The glass samples were presented to the input file as a small cylinder with a diameter of 15 mm and various thicknesses. The detector applied in the immediate simulation has a type of F4 which is tally to predict the number of photons incident per unit detector cell. The NPS was set up to prevent the interaction after 106 historical. The MCNP-5 code employs the primary cross-section data sources ENDF, ACTI, ENDL, ACTI, and T-16 files [32].

The simulated ATL was transferred to the linear attenuation coefficient (LAC, μ). Based on the LAC for the synthesized TZEAg glasses, the transmission rate (TR) was calculated to describe the ratio of photons penetrated the glass thickness, where $TR = (1 - (I/I_0))$. I_0 and I represent the gamma-ray intensities' values before and after passing the glass thickness [33, 34].

3. Result And Discussion

3.1. Mechanical and physical properties

The fabricated glass of ρ (cm^2/g) and V_m (cm^3/mol) were plotted against the Ag_2O insertion content, as illustrated in Figure 2. The ρ values increased systematically between 4.47 and 4.97 g/cm^3 , while the V_m decreased in values between 32.85 to 30.24 cm^3/mol , with increasing Ag_2O insertion ratio from 1 and up to 5 mol%. As the substitution process occurred by the $\text{TeO}_2\text{-ZnO-Er}_2\text{O}_3$ with Ag_2O content, the progress detected in density is due to the partial replacement of TeO_2 , ZnO , and Er_2O_3 with respective densities of 5.67, 5.61, and 8.64 g/cm^3 by Ag_2O , which has a density around 7.14 g/cm^3 .

The measured values of ρ , molecular weight (M , g/mol), and heat of formation (enthalpy) for the glass constating compounds were used to evaluate the constating compounds dissociation energy (G_i , kJ/cm^3). After that, the total dissociation energy (G_t , kJ/cm^3) was calculated, where $G_t = \sum x_i G_i$, x_i represents the constituting compound's molar fraction. The packing factor (V_i , cm^3/mol) was also calculated based on each constituting element's ionic radius. The change in V_i and G_t with the Ag_2O insertion ratio was presented in Figure 3. The V_i values were slightly changed from 13.074 to 13.095 cm^3/mol while the G_t decreased from 53.348 to 52.291 kJ/cm^3 when Ag_2O partially replaced the TeO_2 , Er_2O_3 , and ZnO . This behavior is due to the substitution of a small number of Te-O , Zn-O , and Er-O bonds with Ag-O bonds. The bond dissociation energy of the Te-O , Zn-O , Er-O are 354, 284.1, and 611 kJ/cm^3 , while it is 213 kJ/cm^3 for Ag-O . Thus, the G_t decreases with increasing the Ag_2O content in the fabricated glass samples.

Based on the estimated values of V_i and G_t , the mechanical moduli Young (E), bulk (B), Shear (K), and longitudinal (L) were predicted. Figure 4 displays the change in E , B , K , and L as a function of the Ag_2O content. All of the mechanical moduli are slightly increased with increasing the Ag_2O substitution ratio. The mechanical moduli are slightly increased between 42.460 -45.393 GPa, 20.277-23.538 GPa, 18.445-19.203 Gpa, and 44.870-49.142 GPa for E , B , K , and L moduli, respectively. The slight increase in the mechanical moduli is due to V_i and G_i values with slight variation as the Ag_2O replaced the TeO_2 , ZnO , and Er_2O_3 . The mechanical properties predicted using the M-M model were compared to those measured experimentally by Halimah et al., (2019) [35] and illustrated in Table 2. The data listed in Table 1 showed

agreement between the experimental and M-M model results. This confirms the ability of the M-M model to predict the mechanical properties of such glass systems.

Table 2

The Mechanical and elastic properties were measured experimentally and estimated using the M-M model.

	E (GPa)		B (GPa)		K (GPa)		L (GPa)		σ		H	
	Exp	M-M model	Exp	M-M model	Exp	M-M model						
TZEA _g 1	47.60	42.46	28.69	20.28	19.48	18.45	54.67	44.87	0.22	0.15	3.60	4.29
TZEA _g 2	50.24	43.06	34.47	20.95	19.98	18.60	61.11	45.75	0.25	0.16	3.24	4.25
TZEA _g 3	45.94	43.82	26.29	21.81	19.00	18.80	51.63	46.89	0.20	0.17	3.65	4.20
TZEA _g 4	44.78	44.38	24.20	22.49	18.79	18.95	49.25	47.75	0.19	0.17	3.87	4.16
TZEA _g 5	49.12	45.29	39.22	23.54	19.02	19.20	64.58	49.14	0.29	0.18	2.65	4.11

The values of σ and H are calculated based on the elastic moduli and displayed in Figure 5. The σ increased from 0.15 to 0.18, while the H values decreased from 4.29 to 4.11 GPa with increasing the Ag₂O substituting TeO₂-ZnO Er₂O₃ in the fabricated glass samples. The detected behavior is due to the replacement of many Te-O, Zn-O, Er-O bonds by Ag-O bonds.

The predicted values for shear and longitudinal moduli were utilized to calculate the shear velocity (v_s) and longitudinal velocity (v_l) where $v_l = (L/\rho)^{0.5}$ and $v_s = (K/\rho)^{0.5}$. The calculated values of v_l showed that it takes values of 3168, 3160, 3155, 3147 and 3144 m/s for glass samples with 1, 2, 3, 4, and 5 mol % of the Ag₂O content. Also, v_s takes values of 2031, 2015, 1998, 1982 and 1965 for the same glass samples. The calculated values for v_l and v_s showed agreement with the experimental values reported by Halimah et al., (2019) [35]. For almost all samples except for glass with 2 mol % of the Ag₂O, the experimental results have higher values than the theoretical results.

The fractal bond connectivity (d) is a critical parameter relating to the structure and derived by Bergman and Kantor [36]. It describes information about the glass dimensionality and network crosslinks. The calculated d values are 3.64, 3.55, 3.45, 3.37, and 3.26 for glasses TZEA_g1, TZEA_g2, TZEA_g3, TZEA_g4, and TZEA_g5, respectively. The presented d values are closed to 3. Thus, the fabricated glasses have a 3D layer structure, as reported in ref [37]. In this regard, the evaluated d values were compared to those based on experimental measurements. There is an agreement between the theoretical and experimental d values for glass samples TZEA_g1, TZEA_g3, and TZEA_g4. Still, there is a disagreement for glasses TZEA_g2 and TZEA_g5, where the experimental measurement showed that these glasses are 2D layer structure glasses.

3.2. Shielding features of the studied glass

In recent years the different materials are developed for radiation protection. Among these materials, the researchers are fabricated and modified several glasses forms to enhancement in their ability to attenuate the gamma and neutron radiation. The ability is measured and detected via many shielding factors such as linear attenuation coefficient (LAC), transmission rate (TR), half-value layer (HVL), lead equivalent thickness and the effective removal cross-section (ERSCFN).

Figure. 6 offers the variation of LAC with the incident gamma photon energy (E_γ) and the chemical composition (Ag₂O content mol %) of the studied glasses. It is balanced in Fig. 6 that the decrement of LAC values affected by the increment on E_γ from 0.240 to 1.408 MeV. The high levels are disclosed in the low energy range namely the Photoelectric effect (PE) area. At low energy, 0.240 MeV the LAC rates altered from 1.01 to 1.11 cm⁻¹ for TZEA_g1 and TZEA_g5, respectively. The attenuate incident photons with low energies increase owing to the PE cross-section where ($\sigma_{PE} \propto E^{3.5}$). After that the

incident energy E_γ continuously elevated but the LAC values diminish where the Compton scattering interactions (CS) are dominant in the energy range above 0.1 MeV. The decrement is banded to the CS cross-section which is directly proportional to the reciprocal of the incident photon energy ($\sigma_{CS} \propto E^{-1}$). The increment of E_γ for several MeVs affects emotionally the LAC values to reach the minimum values where at 1.408 MeV, the values are 0.21 cm^{-1} and 0.24 cm^{-1} for TZEAg1 and TZEAg5, respectively.

The doped Ag_2O content in the zinc erbium tellurite glasses also affected by the LAC values at the stationary incident photon energy as displayed in Fig. 6. The LAC values are influenced by the increment of Ag_2O content from 1 to 5 mol % in TZEAg glasses, where the M_w raised from 146.85 to 150.28 g/mol for TZEAg1 and TZEAg5, respectively but Z_{eff} diminished. For instance, the LAC values for the investigated glasses varied progressively in between 0.240 and 1.408 MeV with the following sequences: TZEAg1 ($1.01\text{-}0.21 \text{ cm}^{-1}$) < TZEAg2 ($1.03\text{-}0.22 \text{ cm}^{-1}$) < TZEAg3 ($1.06\text{-}0.226 \text{ cm}^{-1}$) < TZEAg4 ($1.08\text{-}0.231 \text{ cm}^{-1}$) < TZEAg5 ($1.11\text{-}0.240 \text{ cm}^{-1}$). This increment can be associated with the cross-sections PE interactions ($\sigma_{PE} \propto Z_{eff}^{4-5}$, CS interactions ($\sigma_{CS} \propto Z_{eff}$) and PP interactions (Z_{eff}^2). in the studied photon energy ranges. Figure 7 illustrates the difference (Diff %) between the simulated LAC and the calculated using XCOM program. The positive difference was observed at low energy while it increased with the increment of photon energy.

Among the investigated TZEAg glasses, two fabricated (TZEAg1 and TZEAg5) are selected to compare their values of LAC with the commercial SCHOTT market glasses RS253, RS253 G18, RS323 G19, RS 360 and RS 520 [38] at the photon energy of cesium source (0.662 MeV) (Fig. 8). The linear attenuation coefficient (LAC) values for TZEAg1 and TZEAg5 were found to be higher than all commercial glasses except RS 520. Thus, the glasses under study are a candidate for applications in different radiation protection fields.

The half value layer (HVL) is the shielding parameter that was computed to detect the ability of the studied TZEAg glasses to reduce the E_γ in half. The HVL values depend on the E_γ and the density of the investigated glass. Therefore, the materials with the minimum values of HVL are significant and can be employed in the different shielding applications. It is obvious in Fig. 9 that the increment on HVL rates is directly proportional to the elevation of E_γ from 0.015 MeV up to 5 MeV. For instance, at the low E_γ range (0.015-0.08 MeV), the HVL values of TZEAg glasses increase from 0.003 to 0.045 cm for TZEAg1 and from 0.002 to 0.046 cm for TZEAg5. This displays the HVL values also impacted the addition of Ag_2O content in the zinc erbium tellurite glasses.

As can be seen in Fig. 9, the HVL values diminish in all E_γ values with the insertion of Ag_2O content increases from 1 to 5 mol %. The HVL rates dropped from 0.003 to 0.002 cm for TZEAg1 (density- 4.47 g/cm^3) and TZEAg5 (density- 4.97 g/cm^3), respectively. This means that the increase in density of TZEAg glasses leads to the HVL values being reduced. Consequently, TZEAg5 is the best-studied glass material that can be used in shielding applications where the incoming photon will travel for a shorter distance inside the TZEAg5 glass material.

The lead equivalent is a shielding factor describing the ratio of radiation attenuation which fabricated material offered compared to the pure lead element. The lead equivalent was calculated for the fabricated glass samples and presented in Figure 10 as a function of photon energy. Figure 10 showed that the lead equivalent increased with increasing the photon energy between 240 and 1408 keV. This means that the fabricated TZEAg glasses are more shielding effective at the end of the studied range (i.e., 1000 to 1408 keV). The lead equivalent varied between 0.136-0.349, 0.240- 0.358, 0.143- 0.368, 0.146- 0.377, and 0.150 -0.389 for glass samples TZEAg1, TZEAg2, TZEAg3, TZEAg4, and TZEAg5, respectively. The mentioned results also showed that the equivalent lead ratio was enhanced with the addition of Ag_2O content.

The transmission rate (TR) was calculated for the fabricated TZEAg glasses. Figure 11 displays the TR changes versus the Ag_2O content for the TZEAg glasses at different photon energy and glass thickness. Figure 11 depicts that TR values

are affected by the gamma photons energy, glass thickness, and modifier type. Gamma photon energy has the highest effect on the transmission rate, where it is increased with an increase the photon energy. The increase in the TR is related to the incoming photons' penetration power, where the penetration power also increased with an increase in the photon energy. Thus, a thicker thickness is required to stop the gamma photons with high penetration powers. The TR increases between 0.0791, 0.427, 0.564, and 0.584 with increasing in photon energy between 240, 662, 1250, and 1406 keV, respectively, for 2.5 cm thickness of the glass TZEAg1. The TR's increase is linearly in the studied energy region due to the Compton Scattering interaction, which is the primary interaction in the investigated energy interval.

The second important factor affecting the TR is the glass thickness, where thicker glasses are better in stopping the incident radiations. The thicker glass layer strongly forced the gamma photons to interact with glass electrons and atoms; producing a high resistance for the passing photons. Thus, the LAC of the studied glass increase, and the photon TR decreases. At gamma-ray energy 662 keV, Figure 9b showed that the TR decreased from 0.698 to 0.166 with the increase of the glass TZEAg3 thickness from 1 to 5 cm.

Also, the modifier type plays a role in reducing or increasing the TR. Figure 11 a, b, c, **and d** illustrate that the replacement of TeO₂, ZnO, and Er₂O₃ by Ag₂O is slightly reduced the TR values. This is related to the effective atomic number (Z_{eff}) of the fabricated glass samples, where substituting of TeO₂, ZnO, and Er₂O₃ by Ag₂O resulting a slight increase in the Z_{eff} of the fabricated glass. Thus, the LAC of the fabricated glass increases and the photons TR decreased. The TR at energy 240 keV and thickness 1 cm decreased from 0.362 to 0.327, increasing the Ag₂O between 0 and 5 mol%, respectively.

The fast neutron mass removal cross-section \sum_R (cm²/g) was calculated theoretically for the fabricated TZEAg glass samples, as illustrated in Figure 12a. The \sum_R (cm²/g) takes values 0.01902, 0.01898, 0.01893, 0.01888 and 0.01884 cm²/g for glass samples with 1, 2, 3, 4, and 5 mol% of Ag₂O. The reduction in the \sum_R (cm²/g) is due to the replacement of Te, E, and Zn with Ag. The macroscopic cross-section of Te, Er, and Zn are 0.013408, 0.11522, 0.018648 cm²/g, while the Ag macroscopic cross-section is 0.014196 cm²/g.

Based on the calculated effective removal cross-section for the fast neutron, the removal cross-section \sum_R (cm⁻¹) was calculated and plotted versus the glass density, as presented in Figure 12b. The \sum_R (cm⁻¹) increases in the following order 0.08504, 0.08691, 0.08916, 0.09102, and 0.09362 cm⁻¹ with increasing the glass density between 4.47, 4.58, 4.71, 4.82, and 4.97 g/cm³, respectively. Also, the relaxation length (λ , cm) was calculated and presented in Figure 12c versus the Ag₂O content. The λ values decrease from 11.759 cm to 10.681 cm, increasing with the AgO₂ between 1 and 5 mol%, respectively. This decrease is due to the replacement of lower macroscopic cross-section elements Er, Te by a higher element Ag. Also, the thickness required to absorb the half amount of neutrons is calculated and plotted as a function of the material density. It takes values 8.15, 7.97, 7.77, 7.61, and 7.40 cm for samples TZEAg1, TZEAg2, TZEAg3, TZEAg4, and TZEAg5, respectively.

Structural properties

X-ray diffraction

X-ray diffraction or also called XRD is one of the characterizations that is used to study the structural properties of the glass. In this work, the XRD was employed to identify whether the fabricated glass sample is amorphous or crystalline. The XRD spectra of the glass series are illustrated in Figure 12. The spectra were recorded at room temperature in the range of $20^\circ \leq \theta \leq 80^\circ$.

The XRD spectra as depicted in Figure 12 display a broad diffusion hump at the lower scattering angles proposing the presence of a lack of long-range structural order in the glass samples. The existence of a broad hump around $2\theta = 30^\circ$ or

in other words, the absence of a sharp peak ratifies the non-existence of the crystalline phases in the material and affirms that both glass series are completely amorphous [39]. The increasing concentration of the dopant leads to the narrowing of the broad humps. It can also be further studied that the shift of the hump towards a high angle might be due to the lower values of d spacing between atomic levels that decrease the bond length. This statement had been supported by Cai *et al.* (2016) [40] had also reported that the non-existence of long-range atomic arrangement in the glass system proves the amorphous nature of the glass samples.

Fourier transform infrared spectroscopy

Fourier transform infrared (FTIR) is one of the non-destructive methods which provides information regarding the structure and vibrational properties of the elements that exist in the glass system. Nanda *et al.*, (2015) had also reported that FTIR is one of the methods that can be used in determining the functional group of the elements as well as providing information about the vibrational modes of the molecules which exist in the disordered amorphous materials. The observable transmission bands in FTIR spectra attained for both glass series are in the range of 611-616 cm^{-1} which is presented in Figure 14. The assignments of the transmission spectra for silver-doped zinc tellurite glasses are tabulated in Table 3. The positions of the valley are related to the tellurite network as mentioned by Azlan *et al.*, (2015) [41].

Table 3
Assignments of the peaks observed in the FTIR spectra of silver-doped erbium zinc tellurite glasses

FTIR peak position (cm^{-1})	IR assignments
611-616	Stretching vibration of TeO_4 units (Kaur <i>et al.</i> , 2016 and Mahesvaran <i>et al.</i> , 2013)

The transmission band for the pure structural unit of tellurium oxide (TeO_2) is positioned at 640 cm^{-1} . Nevertheless, tellurium oxide subsists two different types of functional groups which are trigonal pyramid (TeO_3) and trigonal bipyramid (TeO_4) (Pavani *et al.*, 2011). The TeO_3 functional groups correspond to the Te-non-bridging oxygen while TeO_4 corresponds to the Te-bridging oxygen. The transmission bands that lie in a range of 611-616 cm^{-1} are explained by the presence of the trigonal bipyramid structural unit [42]. This single band is considered to be broadened with the presence TeO_2 structural unit [43]. On the other hand, the variation in the composition of the glass network might also affect the shifting of the functional group in the disordered amorphous material.

Meanwhile, structural units of zinc oxide, erbium oxide ad silver oxide are also not found in the transmission band of the glass system. The zinc lattice in the glass system is said to be broken down which causes the absence structural unit of zinc oxide as an additional functional group. However, at an early stage, the structural unit of zinc oxide will break down the Te-O-Te bonds that subsequently will form coordination effects known as dangling bond (non-bridging oxygen) forming ($\text{Te-O}^- \dots \text{Zn}^{2+} \dots \text{O-Te}$) bonds. Consequently, this will increase the formation structural unit of the trigonal pyramid but in return will reduce more structural units of trigonal bipyramid in the glass system [44]. The presence of both structural units of erbium oxide and silver oxide are also not evidenced which can be associated with low concentration.

Deconvolution technique

The transmittance results are then converted to absorbance data. The absorbance spectra results will be deconvoluted immediately. The deconvolute data will determine the area of every band which corresponds to each element that exists in the glass system. The deconvolution is implemented by using Origin 6.0 software and the result for deconvolution spectra is illustrated in Figure 14.

The FTIR spectra have been deconvoluted to identify the exact peak positions of the structural units which exist in the prepared glass. The peak position (x_c) and amplitude (A) for all the peaks are observed after the deconvolution process.

Then, the data is tabulated in Table 4. The assignments for each functional group in every element are attained from the deconvoluted FTIR spectra which are based on the information obtained from the literature done by previous researchers.

Table 4

Assignments of the peaks of erbium-doped and silver-doped zinc tellurite glasses using deconvolution technique

FTIR peak position (cm ⁻¹)	IR assignments
642-700	Stretching vibration of TeO ₄ units (Kaur <i>et al.</i> , 2016 and Mahesvaran <i>et al.</i> , 2013)
532-580	Anti-symmetric vibration of Te-O bonds in TeO ₃ units (Ayuni <i>et al.</i> , 2011 and Noorazlan <i>et al.</i> , 2013)
480-560	Stretching vibration of Er-O bonds in Er ₂ O ₃ units (Bosca <i>et al.</i> , 2009)
550-560	Stretching vibration of Ag-O bonds in Ag ₂ O units (Coelho <i>et al.</i> , 2012)

Table 5

Band center, B and band area, A of silver-doped erbium zinc tellurite glasses

Ag ₂ O content	Peak position, B (cm ⁻¹) and band area, A (%)				
0.01	B	619.29	702.58	499.21	611.93
	A	20.93	40.93	58.40	42.97
0.02	B	665.81	752.44	481.00	596.28
	A	40.65	18.82	81.50	32.13
0.03	B	616.60	683.48	500.35	607.07
	A	27.20	57.02	48.60	21.16
0.04	B	650.32	698.81	520.53	618.89
	A	29.58	28.53	46.75	15.15
0.05	B	659.42	744.12	485.13	592.32
	A	36.00	18.55	69.55	25.51
Assignments		TeO ₄	TeO ₃	Er ₂ O ₃	Ag ₂ O

As mentioned earlier, the tellurite-based glasses consist of two structural units which are trigonal pyramid (TeO₃) and trigonal bipyramid (TeO₄). After the deconvolution process, the absorption band for both TeO₃ and TeO₄ groups lies in the range of 532-700 cm⁻¹. The IR bands achieved for TeO₄ stretching vibration are in the range of 532-580 cm⁻¹ [42]. Meanwhile, the structural unit for TeO₃ has been detected to present in the range of 642-700 cm⁻¹ [45–46]. According to Ayuni *et al.*, (2011) [45], the absorption band which lies in the range of 620-660 cm⁻¹ represents the symmetrical vibration of Te-O bonds.

Based on Noorazlan *et al.*, (2013) [46], there is still no presence of ZnO structural unit being formed which consists of ZnO₄ and ZnO₆ after the FTIR spectra have been deconvoluted. As mentioned before, the lattice structural unit of ZnO is broken down which provides no functional group of ZnO in the spectra for both glass series. The structural unit for Er₂O₃ presents in the range around 480 cm⁻¹ and 560 cm⁻¹ respectively. The existence structural unit of erbium oxide in the materials modifies the structure of the tellurite glass network [47] and there is also an existing structural unit of Ag₂O in

the glass system which falls in the range of 550-650 cm^{-1} . According to Coelho *et al.*, (2012) [48], the occurrence of shifting bands is due to the presence structural unit of silver oxide which breaks some of the bonds and modifies the structure of the glass system. The increment of both dopants concentration signifies the change of Te-O bond from TeO_4 to TeO_3 which indicates the creation of NBO's that is followed by the shift of the primary structural unit of TeO_2 to a higher wavenumber. The presence of the TeO_4 structural unit acts as evidence towards the formation of BO's at the same time.

The concentration of the structural units present in both glass systems can be attained using the following equation [49]:

$$N_4 = \frac{A_4}{A_4 + A_3} \quad (1)$$

where A_3 and A_4 represent the areas of TeO_3 and TeO_4 units and N_4 is used to determine the concentration units for TeO_4 or vice versa. The concentration of TeO_4 and TeO_3 units which is presented in both glass series are illustrated in Figure 16.

Figure 16 displays the concentration of TeO_4 and TeO_3 structural units against the molar fraction of silver oxide. The deconvolution process has determined the concentration of both TeO_4 and TeO_3 structural units as expressed in Equation 1. The variation of the concentration is attributed to the conversion of the structural units of TeO_4 to TeO_3 and vice versa. The presence of silver-doped zinc tellurite glass contributes to the changes in the tellurite network. Trigonal pyramid (TeO_3) is assigned to the non-bridging oxygen (NBO) which tends to be converted into trigonal bipyramid (TeO_4) structural units or vice versa as more concentration of dopants are included in the glass system. The role of dopants is strongly related to the concentration of trigonal bipyramid and trigonal pyramid structural units.

Conclusion

A series of zinc erbium tellurite glasses doped with silver oxide and based on the chemical formula $[(\text{TeO}_2)_{0.7}(\text{ZnO})_{0.3}]_{0.96}(\text{Er}_2\text{O}_3)_{0.04}]_{1-y}(\text{Ag}_2\text{O})_y$ where $y = 0.01, 0.02, 0.03, 0.04, 0.05$ was studied. The Makishima-Mackenzie assumptions are applied to theoretically estimate the mechanical properties. All elastic moduli are observed to increase with the increment of silver oxide content in the TZEAg glasses where Young (E), bulk (B), Shear (K), and longitudinal (L) varied between 42.460-45.393 GPa, 20.277-23.538 GPa, 18.445-19.203 GPa, and 44.870-49.142 GPa for TZEAg1 and TZEAg5, respectively. The radiation shielding features were also examined for the TZEAg glasses. The LAC values reached the maximum at low energy 0.240 MeV, altered from 1.01 to 1.11 cm^{-1} for TZEAg1 and TZEAg5, respectively. The substitution of ZnO , TeO_2 and Er_2O_3 with Ag_2O content in TZEAg glasses enhanced the features for gamma and neutron radiation protection where TZEAg5 is the preferable glass to be used in various radiation shielding equipment.

Declarations

Acknowledgment

We would like to expand the gratefulness to the authors of the Deanship of Scientific Research at King Khalid University, Saudi Arabia for funding this work through the General Research Program under grant number G.R.P/78/42. We would like to thank Princess Nourah bint Abdulrahman University Researchers Supporting Project number (PNURSP2022R48), Princess Nourah bint Abdulrahman University, Riyadh, Saudi Arabia.

References

1. A.J. Gislason-Lee, *Patient X-ray exposure and ALARA in the neonatal intensive care unit: Global patterns (Pediatrics & Neonatology, 2020)*

2. C. Rodgerson, ALARA and paediatric imaging in radiation therapy: A survey of Canadian paediatric imaging practice. *Radiography* **20**(3), 183–188 (2014)
3. S. Kaewjaeng, S. Kothan, W. Chaiphaksa, N. Chanthima, R. Rajaramakrishna, H.J. Kim, J. Kaewkhao, High transparency $\text{La}_2\text{O}_3\text{-CaO-B}_2\text{O}_3\text{-SiO}_2$ glass for diagnosis x-rays shielding material application. *Radiat. Phys. Chem.* **160**, 41–47 (2019)
4. N. Chanthima, J. Kaewkhao, P. Limkitjaroenporn, S. Tuscharoen, S. Kothan, M. Tungjai, P. Limsuwan, Development of $\text{BaO-ZnO-B}_2\text{O}_3$ glasses as a radiation shielding material. *Radiat. Phys. Chem.* **137**, 72–77 (2017)
5. A.S. Abouhaswa, E. Kavaz, A novel $\text{B}_2\text{O}_3\text{-Na}_2\text{O-BaO-HgO}$ glass system: Synthesis, physical, optical and nuclear shielding features. *Ceram. Int.* **46**(10), 16166–16177 (2020)
6. B. Aygün, High alloyed new stainless steel shielding material for gamma and fast neutron radiation. *Nuclear Engineering and Technology* **52**(3), 647–653 (2020)
7. B. Aygün, E. Şakar, O. Agar, M.I. Sayyed, A. Karabulut, V.P. Singh, Development of new heavy concretes containing chrome-ore for nuclear radiation shielding applications. *Prog. Nucl. Energy* **133**, 103645 (2021)
8. Y. Al-Hadeethi, M.I. Sayyed, Y.S. Rammah, Fabrication, optical, structural and gamma radiation shielding characterizations of $\text{GeO}_2\text{-PbO-Al}_2\text{O}_3\text{-CaO}$ glasses. *Ceram. Int.* **46**(2), 2055–2062 (2020)
9. Y. Al-Hadeethi, M.I. Sayyed, H. Mohammed, L. Rimondini, X-ray photons attenuation characteristics for two tellurite based glass systems at dental diagnostic energies. *Ceram. Int.* **46**(1), 251–257 (2020)
10. S. Yesmin, B.S. Barua, M.U. Khandaker, M.T. Chowdhury, M. Kamal, M.A. Rashid, D.A. Bradley, Investigation of ionizing radiation shielding effectiveness of decorative building materials used in Bangladeshi dwellings. *Radiat. Phys. Chem.* **140**, 98–102 (2017)
11. S. Yasmin, B.S. Barua, M.U. Khandaker, M.A. Rashid, D.A. Bradley, M.A. Olatunji, M. Kamal, Studies of ionizing radiation shielding effectiveness of silica-based commercial glasses used in Bangladeshi dwellings. *Results in Physics* **9**, 541–549 (2018)
12. Y. Al-Hadeethi, M.I. Sayyed, $\text{BaO-Li}_2\text{O-B}_2\text{O}_3$ glass systems: potential utilization in gamma radiation protection. *Prog. Nucl. Energy* **129**, 103511 (2020)
13. C. Bootjomchai, J. Laopaiboon, C. Yenchai, R. Laopaiboon, Gamma-ray shielding and structural properties of barium–bismuth–borosilicate glasses. *Radiat. Phys. Chem.* **81**(7), 785–790 (2012)
14. S. Yasmin, Z.S. Rozaila, M.U. Khandaker, B.S. Barua, F.U.Z. Chowdhury, M.A. Rashid, D.A. Bradley, The radiation shielding offered by the commercial glass installed in Bangladeshi dwellings. *Radiat. Eff. Defects Solids* **173**(7-8), 657–672 (2018)
15. M.I. Sayyed, K.A. Mahmoud, E. Lacomme, M.M. AlShammari, N. Dwaikat, Y.S.M. Alajerami, M.H.A. Mhareb, Development of a novel MoO_3 -doped borate glass network for gamma-ray shielding applications. *The European Physical Journal Plus* **136**(1), 1–16 (2021)
16. N. Chanthima, J. Kaewkhao, P. Limsuwan, Study of photon interactions and shielding properties of silicate glasses containing Bi_2O_3 , BaO and PbO in the energy region of 1 keV to 100 GeV. *Annals of Nuclear energy* **41**, 119–124 (2012)
17. E. Kavaz, E.H. Ghanim, A.S. Abouhaswa, Optical, structural and nuclear radiation security properties of newly fabricated $\text{V}_2\text{O}_5\text{-SrO-PbO}$ glass system. *J. Non-Cryst. Solids* **538**, 120045 (2020)
18. H. Akyildirim, E. Kavaz, F.I. El-Agawany, E. Yousef, Y.S. Rammah, Radiation shielding features of zirconolite silicate glasses using XCOM and FLUKA simulation code. *J. Non-Cryst. Solids* **545**, 120245 (2020)
19. B. Oto, E. Kavaz, H. Durak, A. Aras, Z. Madak, Effect of addition of molybdenum on photon and fast neutron radiation shielding properties in ceramics. *Ceram. Int.* **45**(17), 23681–23689 (2019)

20. O. Taktak, H. Souissi, S. Kammoun, Optical absorption properties of $\text{ZnF}_2\text{-RO-TeO}_2$ (R= Pb, Cd and Zn) glasses doped with chromium (III): Neuhauser model and crystal field study. *Opt. Mater.* **113**, 110682 (2021)
21. M. Kumar, Y.C. Ratnakaram, Role of TeO_2 coordination with the BaF_2 and Bi_2O_3 on structural and emission properties in Nd^{3+} doped fluoro phosphate glasses for NIR 1.058 μm laser emission. *Optical Materials*, *112*, 110738
22. A.H. Almuqrin, M.I. Sayyed, Radiation shielding characterizations and investigation of $\text{TeO}_2\text{-WO}_3\text{-Bi}_2\text{O}_3$ and $\text{TeO}_2\text{-WO}_3\text{-PbO}$ glasses. *Appl. Phys. A* **127**(3), 1–11 (2021)
23. M. Ennouri, L. Kuusela, I. Jlassi, B. Gelloz, L. Petit, H. Elhouichet, Impact of Ag_2O Content on the Optical and Spectroscopic Properties of Fluoro-Phosphate Glasses. *Materials* **12**(21), 3516 (2019)
24. M.I. Sayyed, M. Rashad, Y.S. Rammah, Impact of Ag_2O on linear, nonlinear optical and gamma-ray shielding features of ternary silver vanadio-tellurite glasses: $\text{TeO}_2\text{-V}_2\text{O}_5\text{-Ag}_2\text{O}$. *Ceram. Int.* **46**(14), 22964–22972 (2020)
25. N. Baizura, A.K. Yahya, Effects of Nb_2O_5 Replacement by Er_2O_3 on elastic and structural properties of $75\text{TeO}_2\text{-(10-x)Nb}_2\text{O}_5\text{-15ZnO-(x)Er}_2\text{O}_3$ glass. *J. Non-cryst. Solids* **357**(15), 2810–2815 (2011)
26. O. Agar, E. Kavaz, E.E. Altunsoy, O. Kilicoglu, H.O. Tekin, M.I. Sayyed, ... N. Tarhan, Er_2O_3 effects on photon and neutron shielding properties of $\text{TeO}_2\text{-Li}_2\text{O-ZnO-Nb}_2\text{O}_5$ glass system. *Results in Physics* **13**, 102277 (2019)
27. A. Sharma, B. Singh, B.S. Sandhu, Investigation of photon interaction parameters of polymeric materials using Monte Carlo simulation. *Chin. J. Phys.* **60**, 709–719 (2019)
28. A. Sharma, B. Singh, B.S. Sandhu, A Compton scattering technique for wood characteristics using FLUKA Monte Carlo code. *Radiat. Phys. Chem.* **182**, 109364 (2021)
29. M.I. Sayyed, K.A. Mahmoud, O.L. Tashlykov, M.U. Khandaker, M.R.I. Faruque, Enhancement of the Shielding Capability of Soda–Lime Glasses with Sb_2O_3 Dopant: A Potential Material for Radiation Safety in Nuclear Installations. *Applied Sciences* **11**(1), 326 (2021)
30. G. Yankov, L. Dimowa, N. Petrova, M. Tarassov, K. Dimitrov, T. Petrov, B.L. Shivachev, Synthesis, structural and non-linear optical properties of $\text{TeO}_2\text{-GeO}_2\text{-Li}_2\text{O}$ glasses. *Opt. Mater.* **35**(2), 248–251 (2012)
31. A. El-Adawy, N. El-Kheshkhany, Effect of rare earth (Pr_2O_3 , Nd_2O_3 , Sm_2O_3 , Eu_2O_3 , Gd_2O_3 and Er_2O_3) on the acoustic properties of glass belonging to bismuth–borate system. *Solid State Commun.* **139**(3), 108–113 (2006)
32. F.B. Brown (2003). MCNP—a general Monte Carlo N-particle transport code, version 5. *Los Alamos National Laboratory, Oak Ridge, TN*
33. K.A. Mahmoud, M.I. Sayyed, A.M. Alhuthali, M.Y. Hanfi (2020). The effect of CuO additive on the mechanical and radiation shielding features of $\text{Li}_2\text{B}_4\text{O}_7\text{-Pb}_2\text{O}_3$ glass system. *Boletín de la Sociedad Española de Cerámica y Vidrio*
34. K.M. Kaky, M.I. Sayyed, M.H.A. Mhareb, A.H. Abdalsalam, K.A. Mahmoud, S.O. Baki, M.A. Mahdi, Physical, structural, optical and gamma radiation attenuation properties of germanate-tellurite glasses for shielding applications. *J. Non-Cryst. Solids* **545**, 120250 (2020)
35. M.K. Halimah, S.N. Nazrin, F.D. Muhammad (2019). Influence of silver oxide on structural, physical, elastic and optical properties of zinc tellurite glass system for optical application. *Chalcogenide Letters*, *16*(8)
36. D.J. Bergman, Y. Kantor, Critical properties of an elastic fractal. *Physical review letters* **53**(6), 511 (1984)
37. S.H. Alazoumi, H.A.A. Sidek, M.K. Halimah, K.A. Matori, M.H.M. Zaid, A.A. Abdulbaset (2017). Synthesis and elastic properties of ternary ZnO-PbO-TeO_2 glasses. *Chalcogenide Letters*, *14*(8)
38. V.V. Cay, M. Sutcu, O. Gencel, T. Korkut (2014). Neutron radiation tests about FeCr slag and natural zeolite loaded brick samples. *Science and Technology of Nuclear Installations*, *2014*
39. Z.A.S. Mahraz, M.R. Sahar, S.K. Ghoshal, M.R. Dousti, Concentration dependent luminescence quenching of Er^{3+} -doped zinc boro-tellurite glass. *Journal of luminescence* **144**, 139–145 (2013)

40. M. Cai, B. Zhou, Y. Tian, J. Zhou, S. Xu, J. Zhang, Broadband mid-infrared 2.8 μm emission in $\text{Ho}^{3+}/\text{Yb}^{3+}$ -codoped germanate glasses. *J. Lumin.* **171**, 143–148 (2016)
41. M.N. Azlan, M.K. Halimah, S.Z. Shafinas, W.M. Daud, Electronic polarizability of zinc borotellurite glass system containing erbium nanoparticles. *Materials Express* **5**(3), 211–218 (2015)
42. P. Kaur, D. Singh, T. Singh, Heavy metal oxide glasses as gamma rays shielding material. *Nucl. Eng. Des.* **307**, 364–376 (2016)
43. M.R. Dousti, M.R. Sahar, S.K. Ghoshal, R.J. Amjad, A.R. Samavati, Effect of AgCl on spectroscopic properties of erbium doped zinc tellurite glass. *Journal of molecular structure* **1035**, 6–12 (2013)
44. Y.B. Saddeek, E.R. Shaaban, H.M. Moustafa, Spectroscopic properties, electronic polarizability, and optical basicity of $\text{Bi}_2\text{O}_3\text{-Li}_2\text{O-B}_2\text{O}_3$ glasses. *Physica B* **403**(13-16), 2399–2407 (2008)
45. J.N. Ayuni, M.K. Halimah, Z.A. Talib, H.A.A. Sidek, W.M. Daud, A.W. Zaidan, A.M. Khamirul (2011, February). Optical properties of ternary $\text{TeO}_2\text{-B}_2\text{O}_3\text{-ZnO}$ glass system. In *IOP Conference Series: Materials Science and Engineering* (Vol. 17, No. 1, p. 012027). IOP Publishing
46. A. Muhammad Noorazlan, M. Kamari, H. Zulkefly, S. S., & D.W. Mohamad (2013). Effect of erbium nanoparticles on optical properties of zinc borotellurite glass system. *Journal of Nanomaterials*, 2013
47. M. Bosca, L. Pop, G. Borodi, P. Pascuta, E. Culea, XRD and FTIR structural investigations of erbium-doped bismuth–lead–silver glasses and glass ceramics. *J. Alloys Compd.* **479**(1-2), 579–582 (2009)
48. J. Coelho, C. Freire, N.S. Hussain, Structural studies of lead lithium borate glasses doped with silver oxide. *Spectrochim. Acta Part A Mol. Biomol. Spectrosc.* **86**, 392–398 (2012)
49. M.A.K. El-Fayoumi, M. Farouk, Structural properties of Li–borate glasses doped with Sm^{3+} and Eu^{3+} ions. *J. Alloys Compd.* **482**(1-2), 356–360 (2009)

Figures

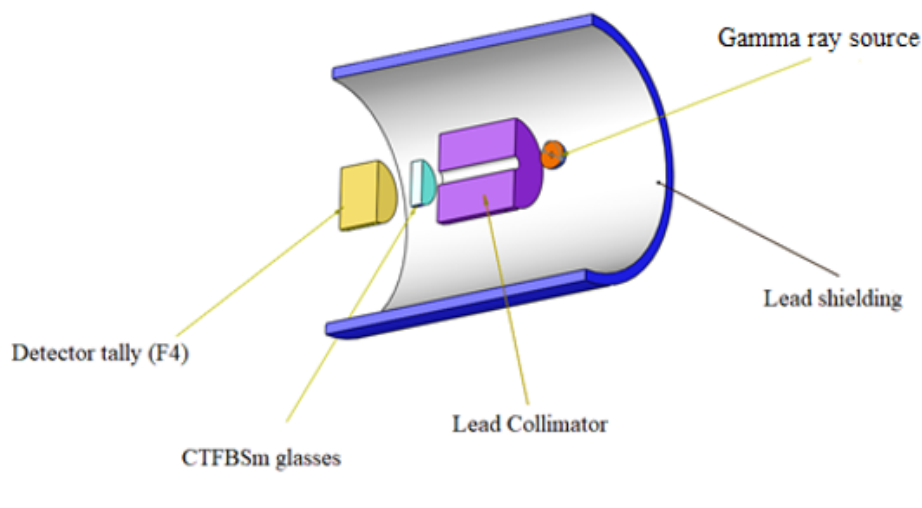


Figure 1

The 3D geometry representing the input file used in the present simulation.

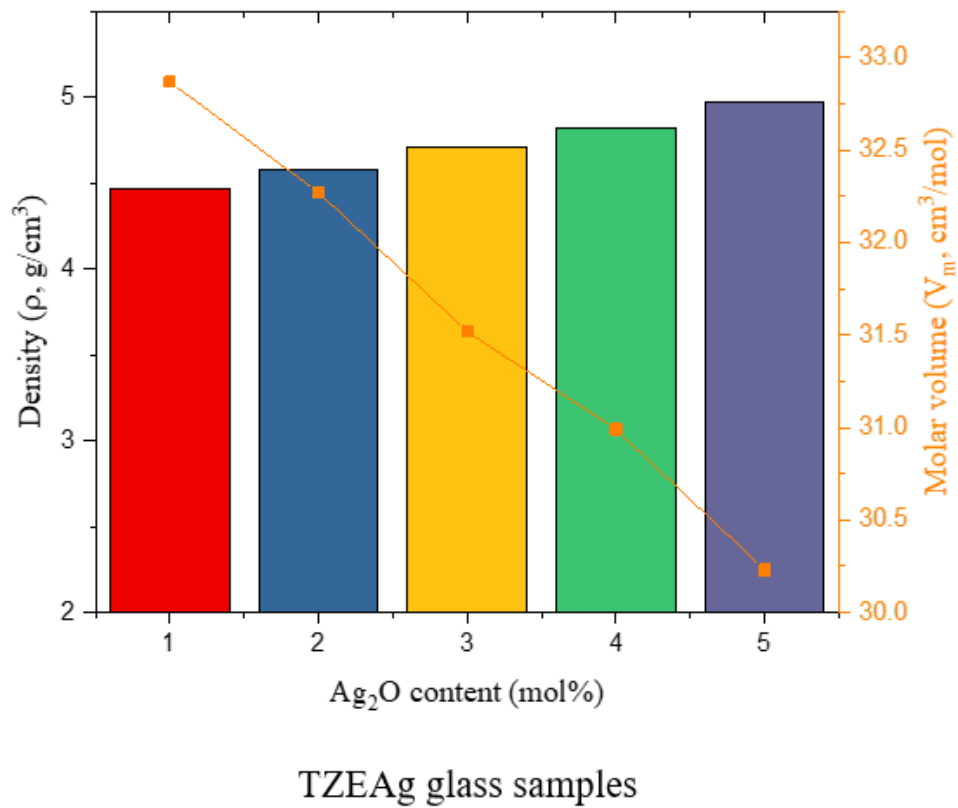


Figure 2

The density and molar volume of the fabricated

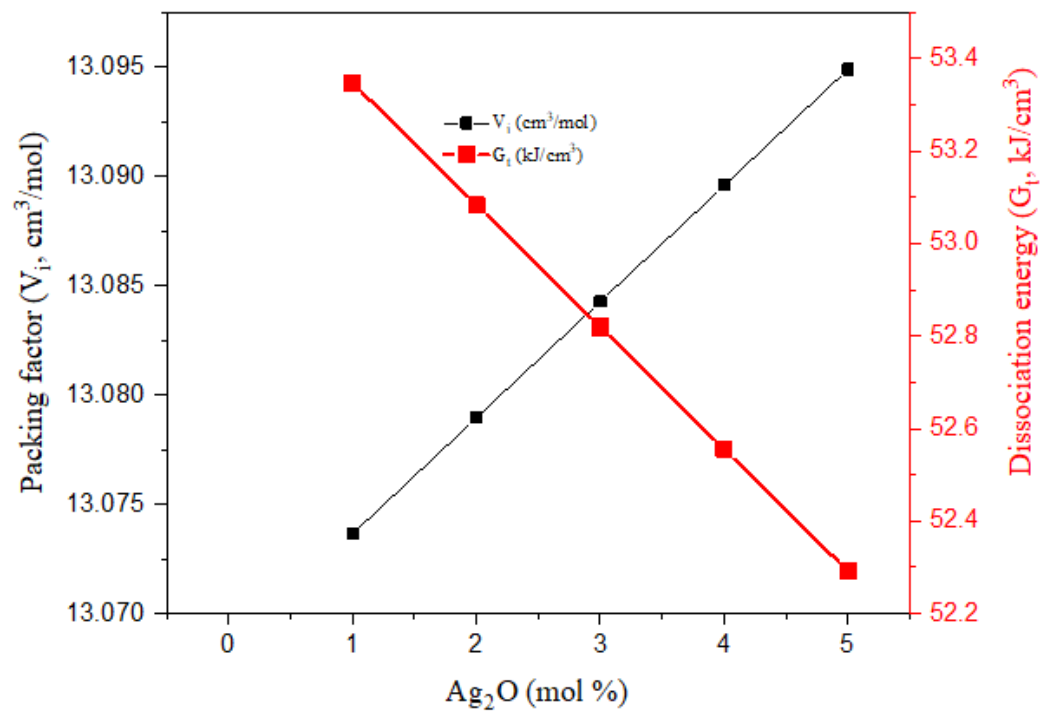


Figure 3

Variation of the packing factor (V_i , cm^3/mol) and dissociation energy (G_f , kJ/cm^3) versus the Ag_2O insertion ratio.

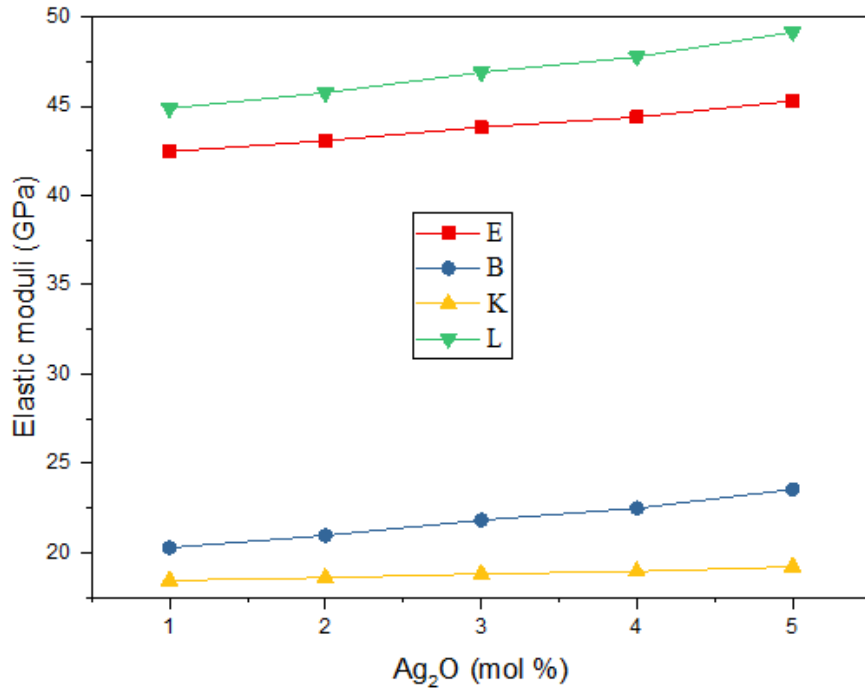


Figure 4

The elastic moduli (Y, B, S, and longitudinal) at different concentrations of Ag_2O .

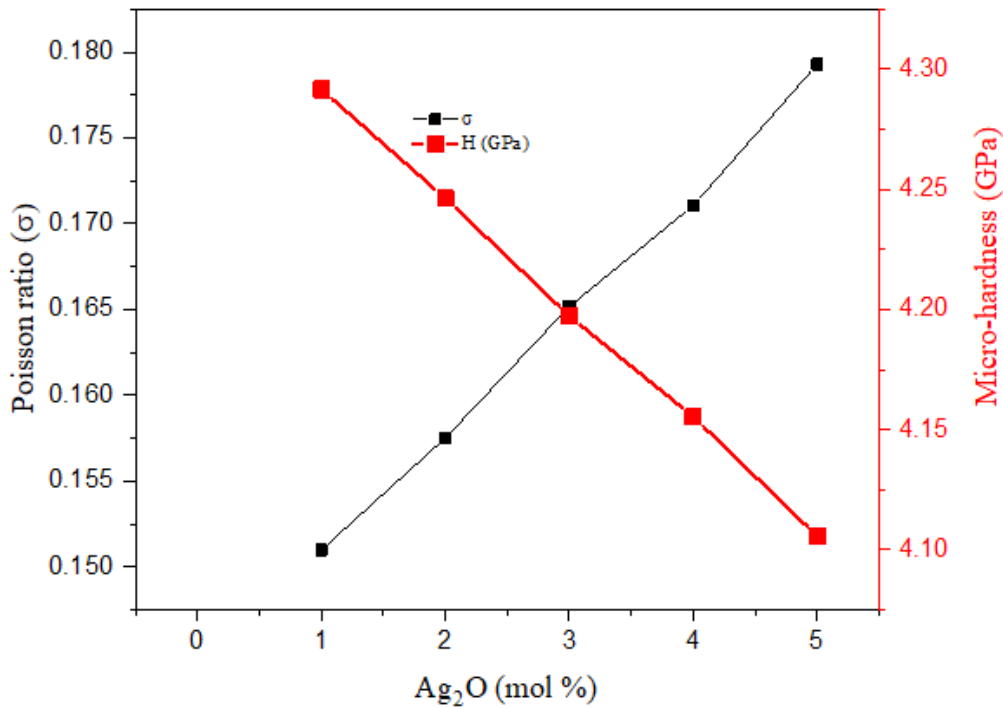


Figure 5

Figure 6

Variation of the linear attenuation coefficient of the fabricated TZEAg glasses versus the gamma photon energy and Ag_2O content.

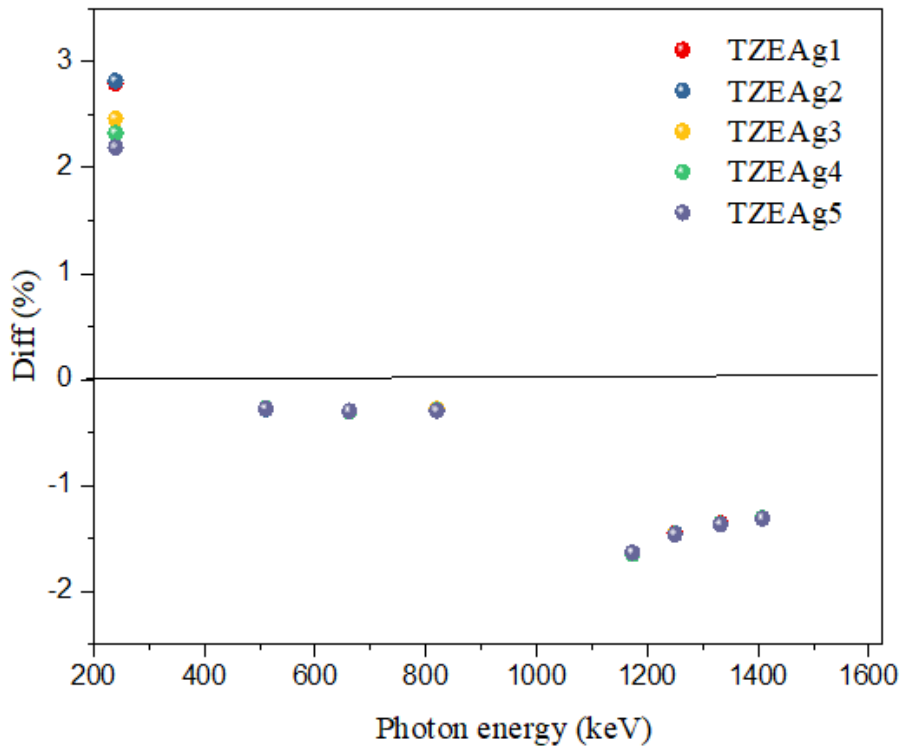


Figure 7

The variance between the LAC simulated using MCNP-5 simulation code and calculated theoretically using the XCOM database.

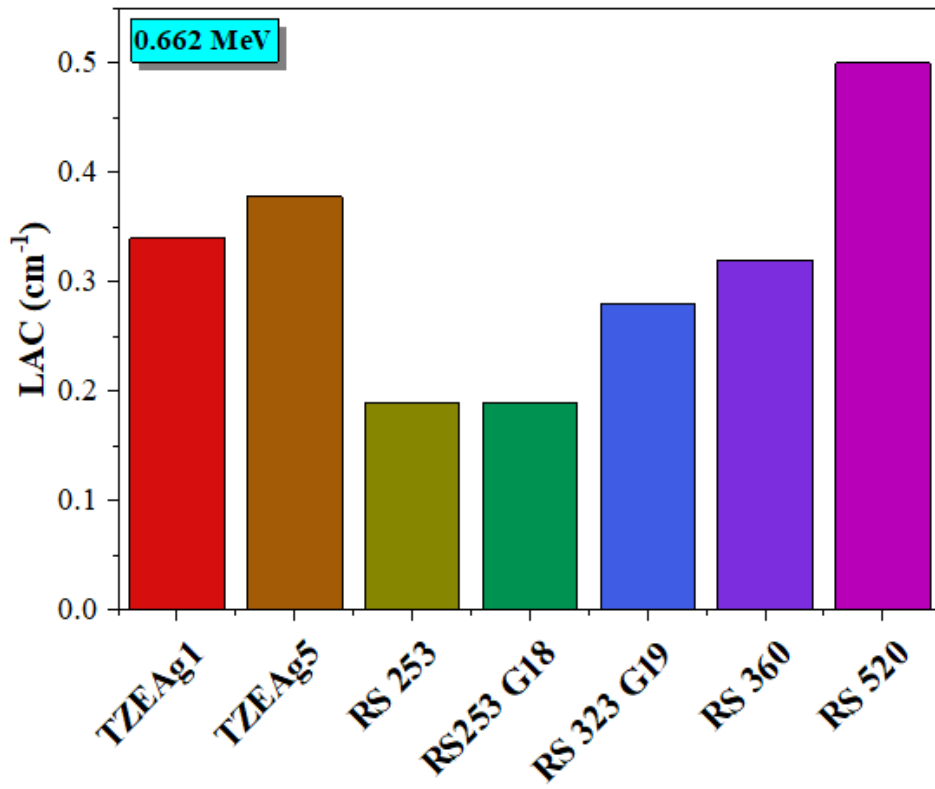


Figure 8

Comparison between studied glasses on their values of LAC with the commercial SCHOTT market glasses at the photon energy of cesium source (0.662 MeV)

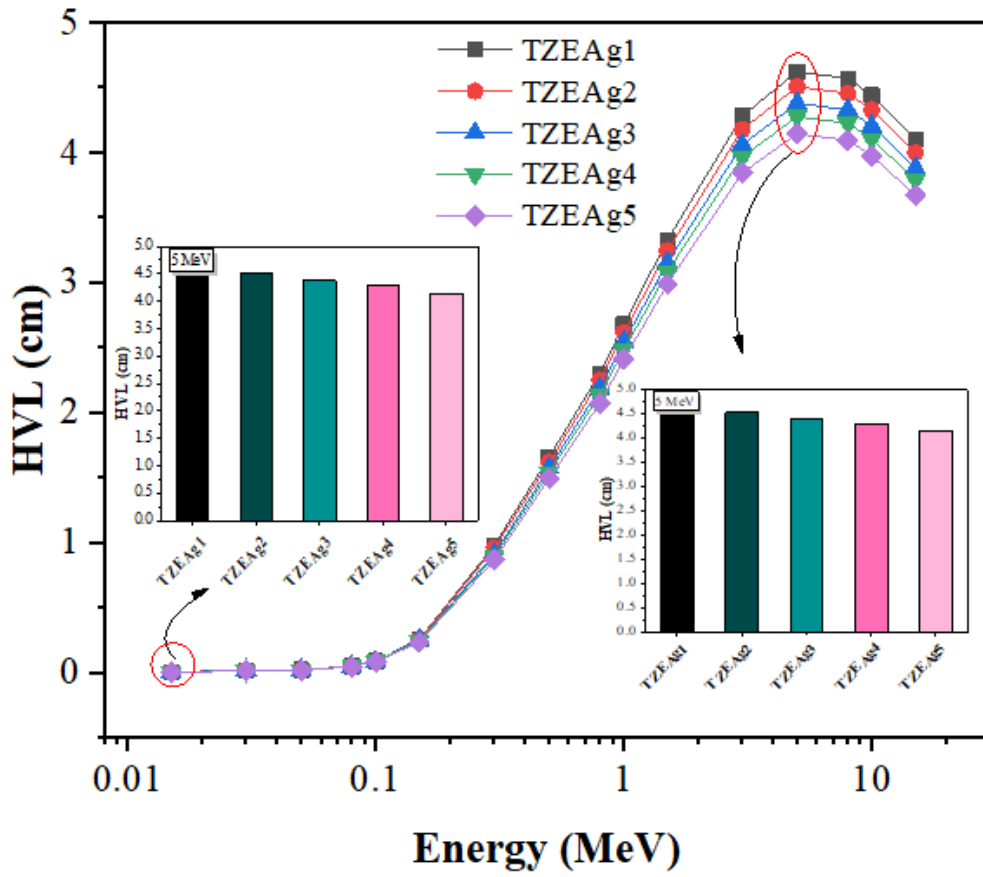


Figure 9

The alteration of HVL values against the photon energy.

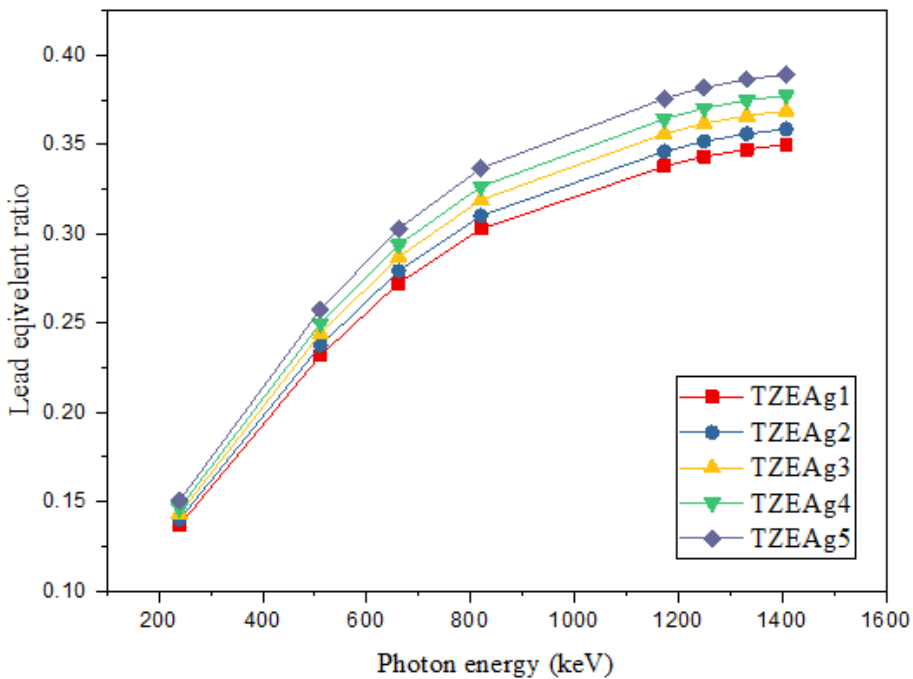


Figure 10

The equivalent lead ratio as a function of the gamma photon energy for the TZEAg glass samples.

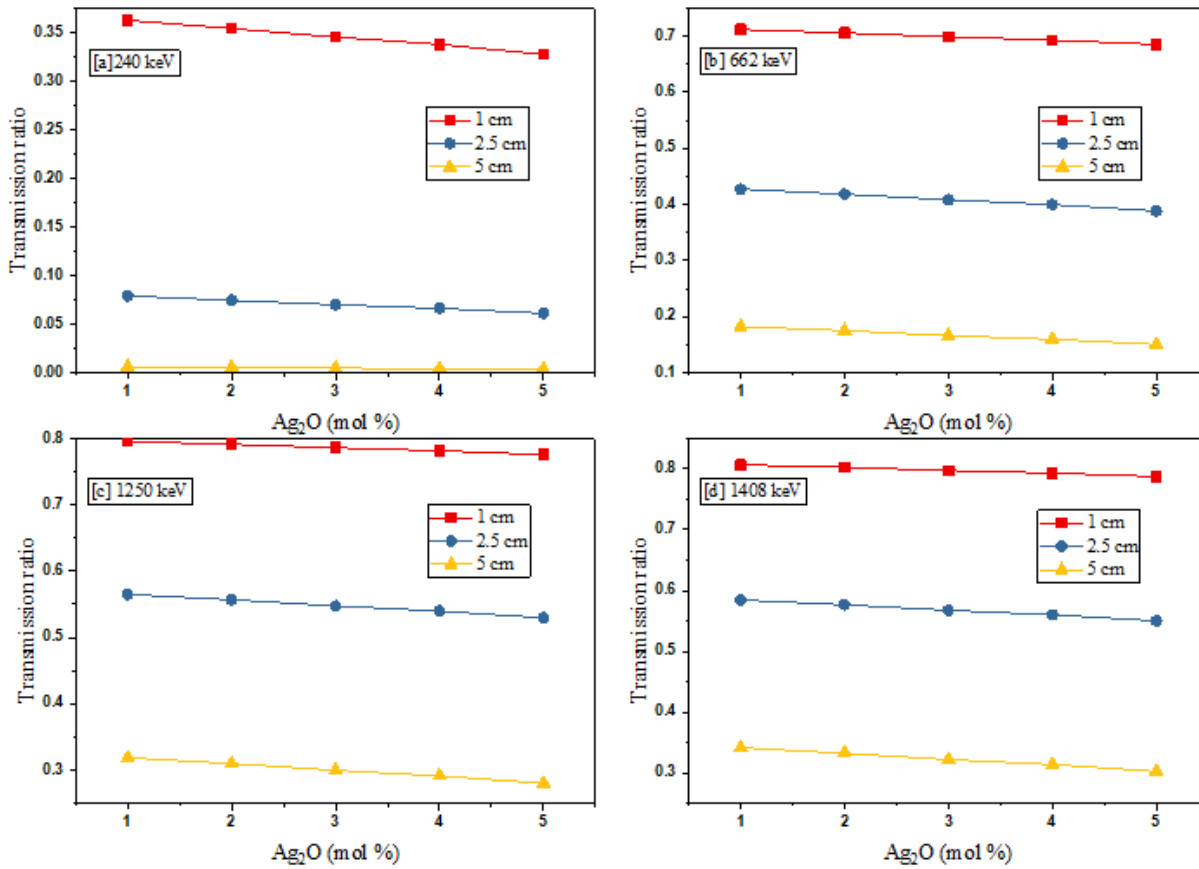


Figure 11

The gamma-ray transmission ratio as a function of Ag_2O content at various glass thickness

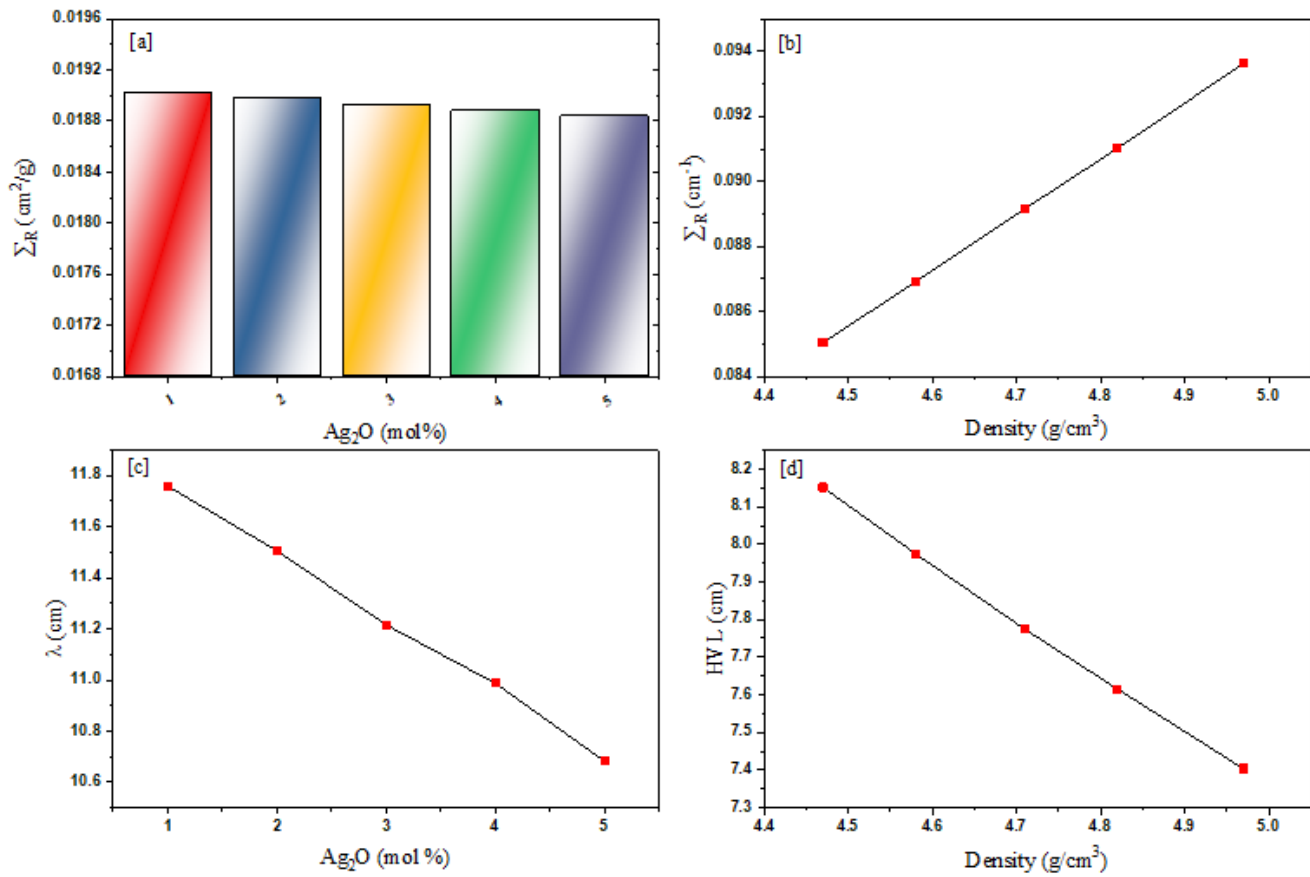


Figure 12

The fast neutron shielding properties [a] The mass removal cross-section Σ_R (cm²/g), [b] the removal cross section Σ_R (cm⁻¹), [c] Relaxation length λ (cm), and [d] the HVL (cm).

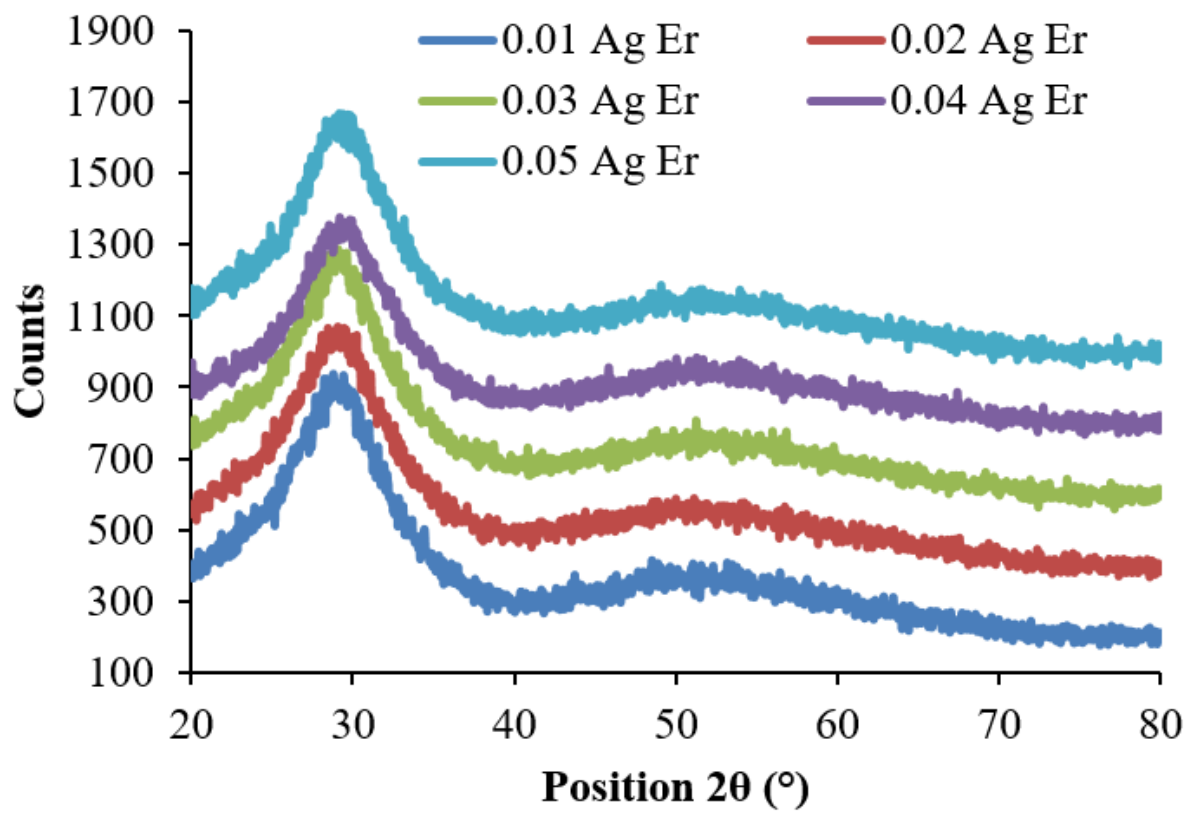


Figure 13

XRD patterns of silver-doped erbium zinc tellurite glasses

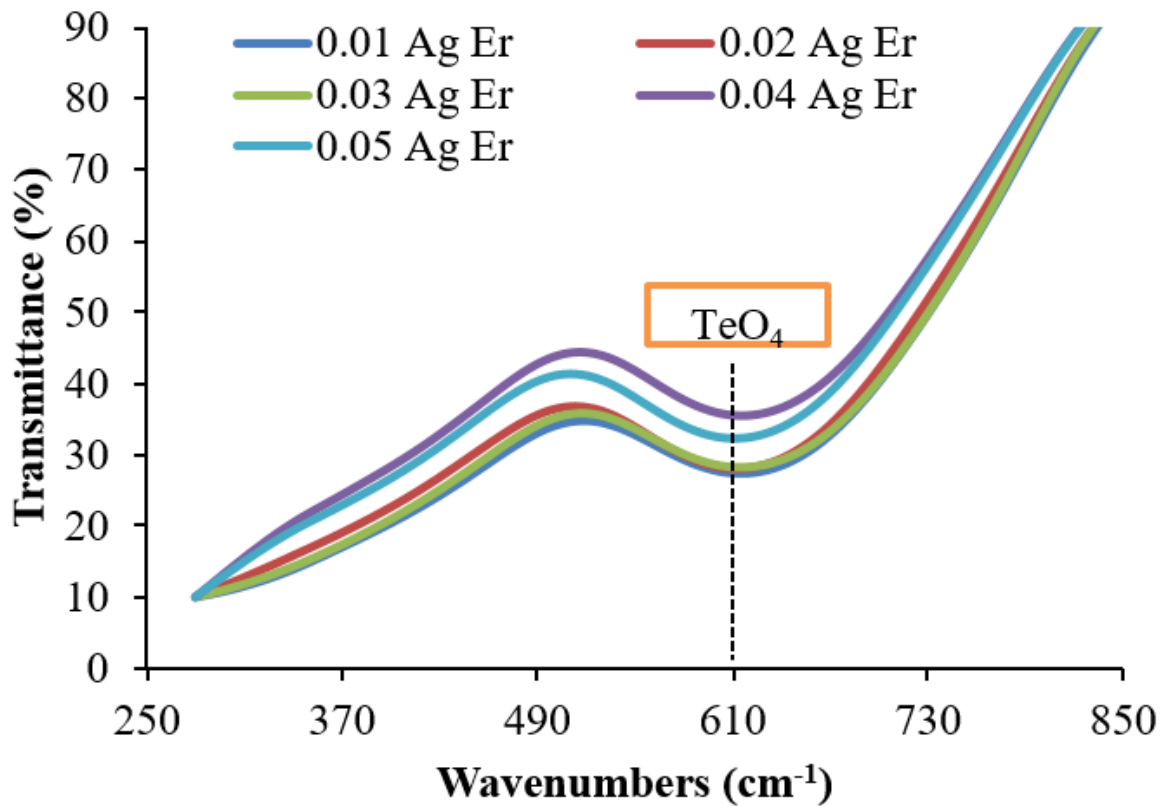


Figure 14

FTIR spectra of silver-doped erbium zinc tellurite glasses

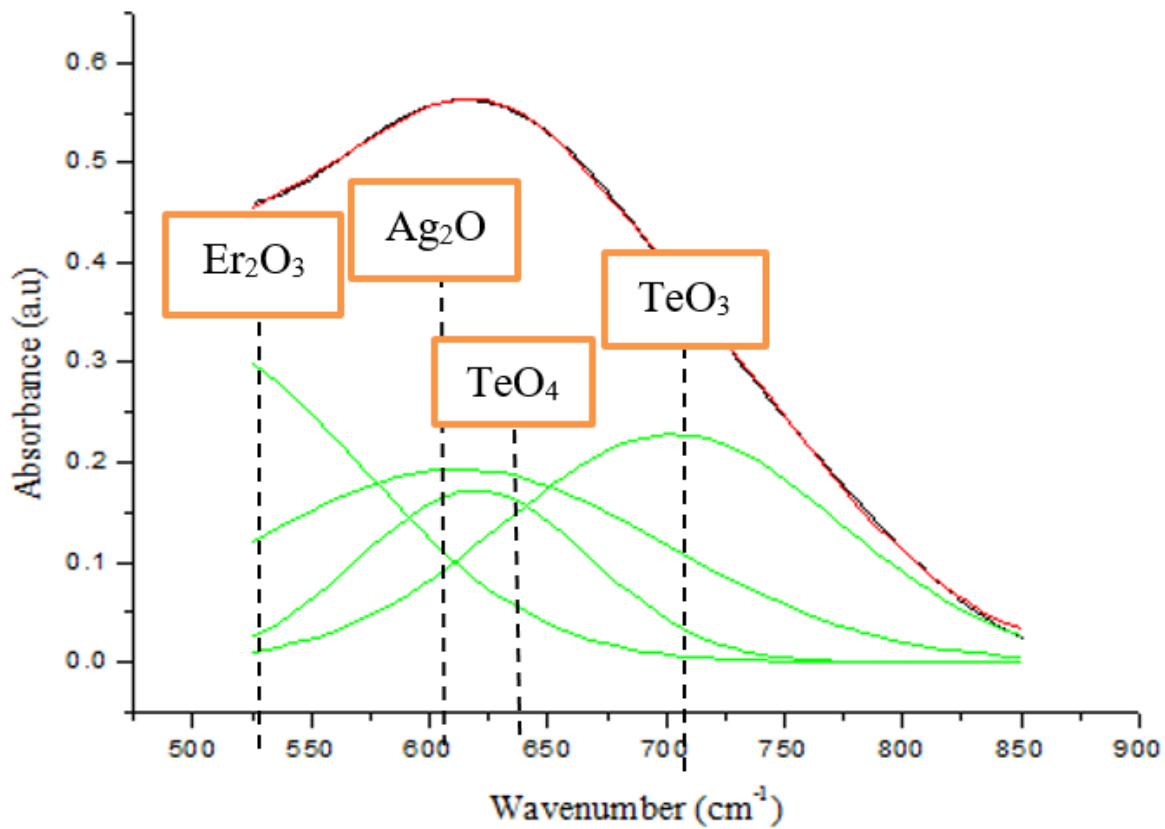


Figure 15

Deconvolution of FTIR spectra of silver-doped erbium zinc tellurite glasses

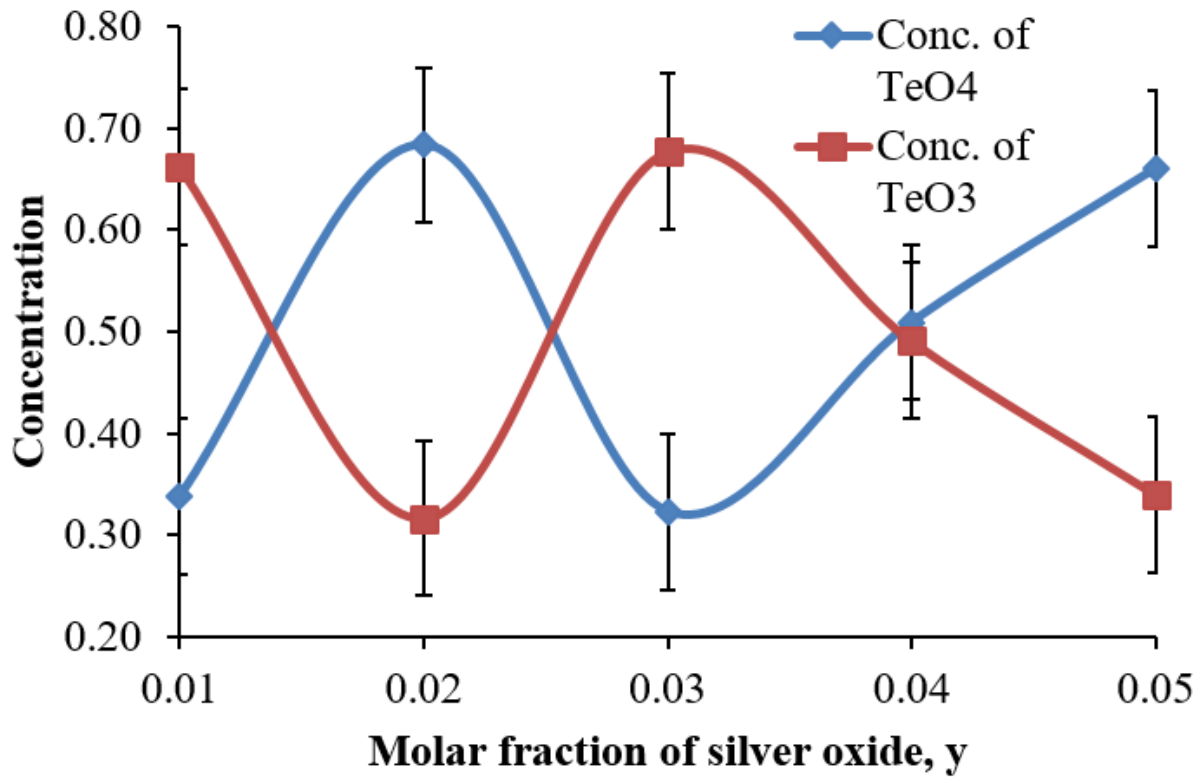


Figure 16

Concentration of TeO₄ and TeO₃ structural units of silver-doped erbium zinc tellurite glasses